Original Paper

Mechanism and reservoir simulation study of the autothermic pyrolysis in-situ conversion process for oil shale recovery

Wei Guo [a, b, c, d], Qiang Li [a, b, c, d], Sun-Hua Deng [a, b, c, d], Yuan Wang [a, b, c, d], Chao-Fan Zhu [a, b, c, d, *]

[a] College of Construction Engineering, Jilin University, Changchun, Jilin, 130026, China
[b] National-Local Joint Engineering Laboratory of In-situ Conversion, Drilling and Exploitation Technology for Oil Shale, Changchun, Jilin, 130021, China
[c] Provincial and Ministerial Co-construction of Collaborative Innovation Center for Shale Oil & Gas Exploration and Development, Changchun, Jilin, 130021, China
[d] Key Laboratory of Drilling and Exploitation Technology in Complex Condition, Ministry of Land and Resource, Changchun, Jilin, 130026, China

A B S T R A C T

The autothermic pyrolysis in-situ conversion process (ATS) consumes latent heat of residual organic matter after kerogen pyrolysis by oxidation reaction, and it has the advantages of low development cost and exploitation of deep oil shale resources. However, the heating mechanism and the characteristic of different reaction zones are still unclear. In this study, an ATS numerical simulation model was proposed for the development of oil shale, which considers the pyrolysis of kerogen, high-temperature oxidation, and low-temperature oxidation. Based on the above model, the mechanism of the ATS was analyzed and the effects of preheating temperature, O_2 content, and injection rate on recovery factor and energy efficiency were studied. The results showed that the ATS in the formation can be divided into five characteristic zones by evolution of the oil and O_2 distribution, and the solid organic matter, including residue zone, autothermic zone, pyrolysis zone, preheating zone, and original zone. Energy efficiency was much higher for the ATS than for the high-temperature nitrogen injection in-situ conversion process (HNICP). There is a threshold value of the preheating temperature, the oil content, and the injection rate during the ATS, which is 400 °C, 0.18, and 1100 m^3/day, respectively, in this study.

1. Introduction

Oil shale, as one of the most important fossil fuels, has plenty of resources. It is an important replacement resource for conventional oil and gas (Dammer et al., 2007). New estimates of oil reserves go up to 47.644 billion tonnes from oil shale in China, and 45% is found in Songliao Basin, especially in the Qingshankou formation of the Southern Songliao Basin (Liu et al., 2009). Despite vast reserves of oil shale, only a small amount of shallow oil shale (<100 m) has been developed by the surficial retorting processing technique, which is harmful to the environment (Zou and Qiu, 2021). If an oil shale formation is artificially heated underground, the kerogen will convert to oil and natural gas in-situ, which is called the oil shale in-situ conversion process (ICP) (Sun et al., 2021). However, the technology has not yet reached the level of industrial development.

This technology has the advantages of green environmental protection, small footprint, low development cost and potential for exploitation of deep oil shale resources, which is an important trend in the oil shale industry.

According to the heat source and transfer mode, there are four technical routes for the realization of oil shale ICP: conduction heating technology, convection heating technology, radiation heating technology, and reaction heat heating technology (Wang et al., 2013). The conduction heating technology and reaction heat heating technology are relatively mature, which have been tested by pilot field tests, and a small amount of oil has been produced (Aouizerate et al., 2012). Small well spacing electric heating technology is a famous conduction heating technology, which has come up by Shell (Meijssen et al., 2014). Small well spacing electric heating technology, which has considerable energy efficiency (3.1), has been successfully executed in the Green River basin of Wyoming and Jordan. Convective heating technology uses high-temperature fluids such as steam and supercritical CO_2 to heat oil shale formation, which heats quickly (Kang et al., 2020). Radiation

* Corresponding author. College of Construction Engineering, Jilin University, Changchun, Jilin, 130026, China.
  E-mail address: chaofan_zhu@jlu.edu.cn (C.-F. Zhu).

Nomenclature

|			
a_1, a_2, b_1, b_2	Fitting parameters	N_{og}	Thermal power of gas and oil, kJ/day
A	Frequency factor, 1/s	p_{in}	Injection pressure, MPa
c	Specific heat capacity of nitrogen, kJ/(kg °C)	p_{sc}	Atmospheric pressure, MPa
C_k	Concentration of kerogen in the pore, mol/m^3	q	Volumetric flow rate of N$_2$, m^3/day
E	Activation energy, kJ/mol	Q	Injection rate, m^3/day
f_h	Heat energy efficiency	R	Ideal gas constant, kJ/(mol K)
f_{og}	Oil-gas energy efficiency	T	Absolute temperature, K
F_{O_2}	O$_2$ content of the gas	ΔT	Temperature variations of nitrogen, °C
k_A	Arrhenius rate constant, 1/s	TOC	Total organic carbon content, wt%
m_k	Mass of organic matter in shale, kg	V_k	Volume of kerogen, m^3
m_k'	Mass of organic matter per mass of shale sample, kg/kg	V_t	Volume of shale, m^3
		γ_C	Mass fraction of C in the kerogen
m_t	Mass of shale sample, kg	ρ	Density of nitrogen, kg/m^3
M_k	Molecular weight of kerogen, g/mol	ρ_t	Density of oil shale, kg/m^3
N_c	Power of isothermal compression, kJ/day	ρ_{in}	Density of inorganic matter, kg/m^3
N_h	Heat power of gas, kJ/day	ρ_k	Density of kerogen, kg/m^3
N_h^{in}	Heat energy of injection gas, kJ/day	φ	Total porosity for the matrix
N_h^{out}	Heat energy of production gas, kJ/day	φ_{oe}	Original effective porosity for the matrix
		φ_k	Porosity of kerogen in the shale
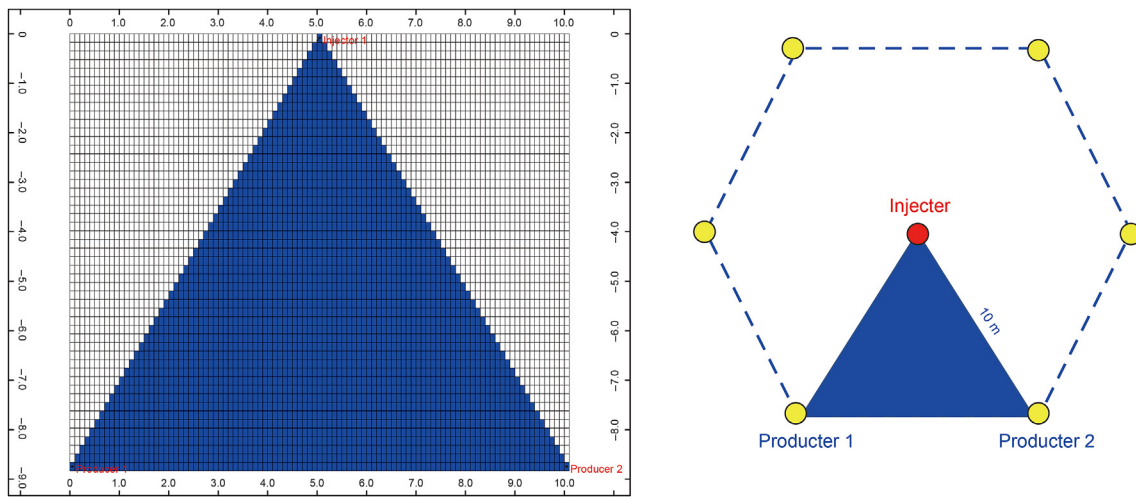
Fig. 1. Schematic diagram of the simulation model and the geo-model grid for the ATS adopted in this study.
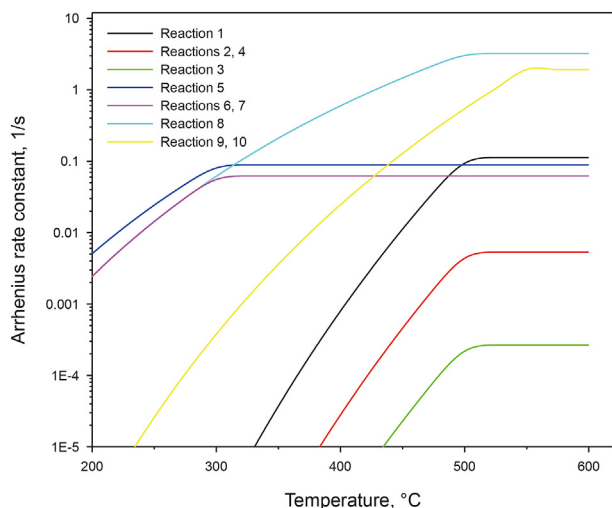

Fig. 2. The relationship between the Arrhenius rate constant of different reactants and temperature.

heating technology heats the formation through an underground radio frequency transmitter. This technology has high heating efficiency and uniform heating, but the downhole equipment is complex and the heating range is limited (Burnham and McConaghy, 2006).

Reaction heating technology is different from the above three physical heating technologies. Most of the heat of kerogen pyrolysis is provided by the oxidation reaction of char, asphaltene, and a small amount of hydrocarbon, which is supplied by the pyrolysis of kerogen (Lee et al., 2014). According to the formation property, natural gas may be injected into the formation to increase the oxidation heat volume. The reaction heating technology can be divided into underground combustion heating technology and autothermic pyrolysis heating technology. Early field tests of oil shale ICP in the United States mainly adopted a combination of underground blasting and underground combustion heating technology (Congress, 1980). The ATS is trigged by injecting room temperature oxygen-containing gas into a locally preheated oil shale formation (Sun et al., 2015b). Compared with underground combustion
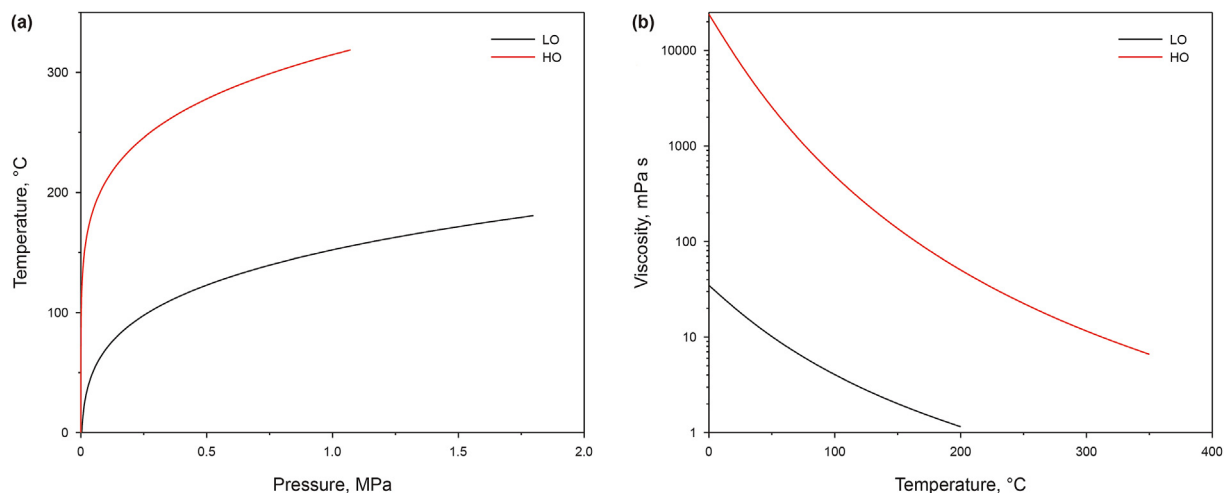
Fig. 3. The phase state and viscosity of HO and LO at different temperatures and pressures: (a) Phase diagram; (b) Viscosity.
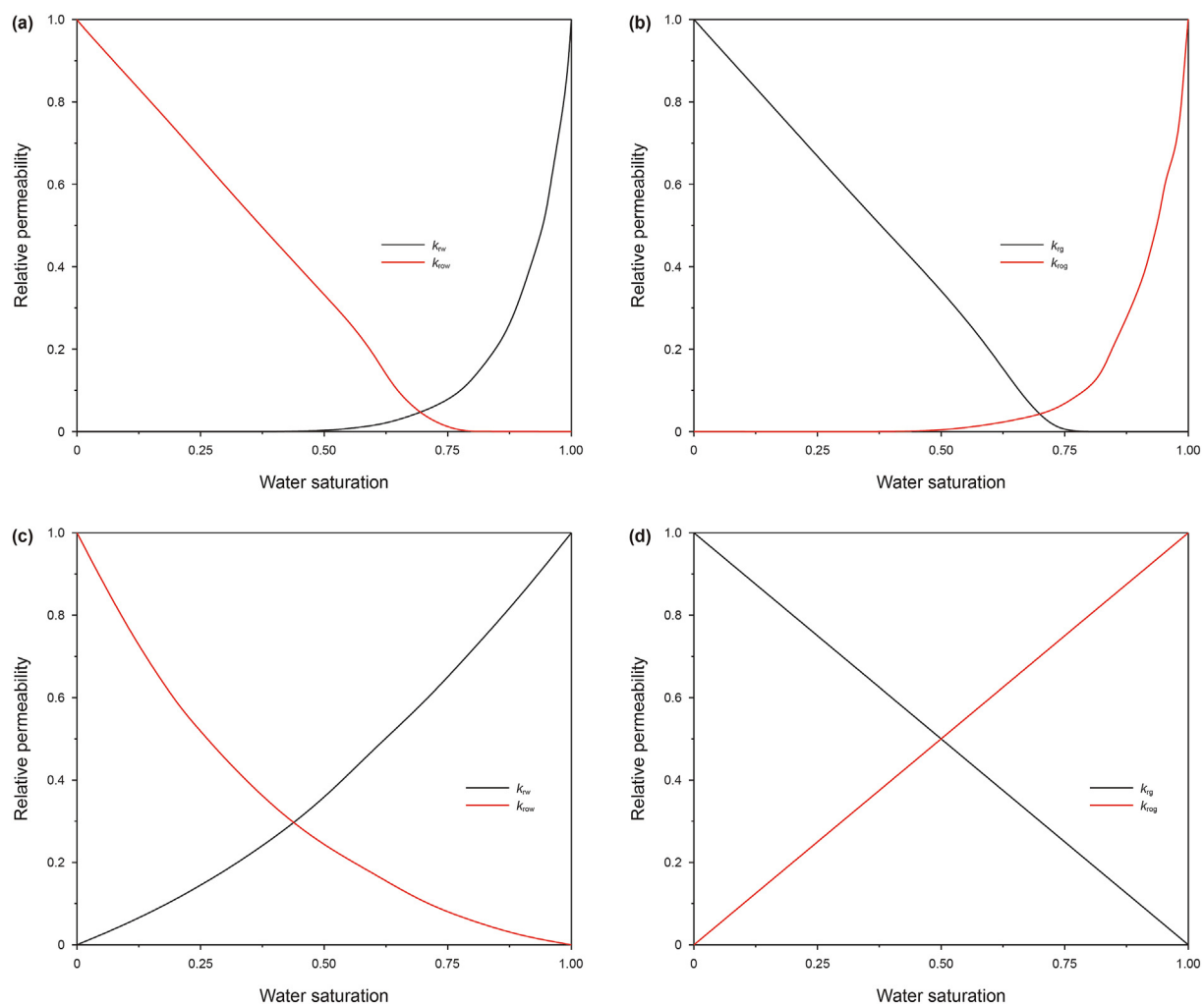

Fig. 4. Relative permeability curves of the shale (Ma, 2015; Pei et al., 2018): (a) Oil-water relative permeability for the matrix; (b) Gas-liquid relative permeability for the matrix; (c) Oil-water relative permeability for the fracture; (d) Gas-liquid relative permeability for the fracture.

heating, the oxidation reaction intensity of autothermic pyrolysis is weak, which reduces heat waste caused by the reaction of oil and gas and inorganic substances in the formation (Sun et al., 2021).

Air at 300 °C and 25 °C was injected into packing oil shale particles by Bai (2015), who examined the ATS in the laboratory. Guo et al., (2016) pointed out that the heat of ATS mainly comes
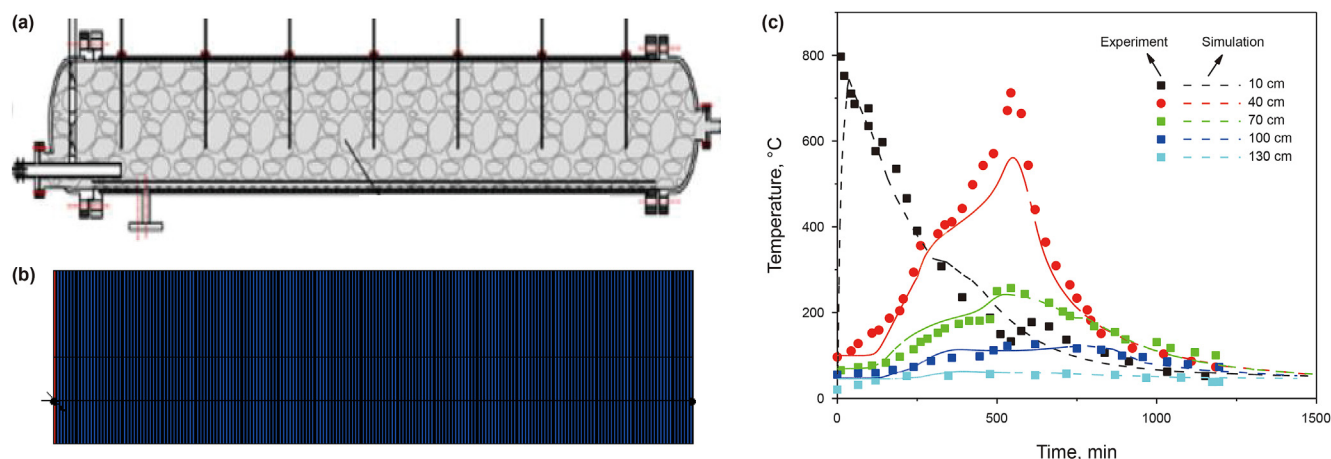
Fig. 5. Model validation: (a) Highly instrumented fixed bed; (b) Simulation model; (c) Data fitting of the temperature evolution during the autothermic pyrolysis laboratory experiment.
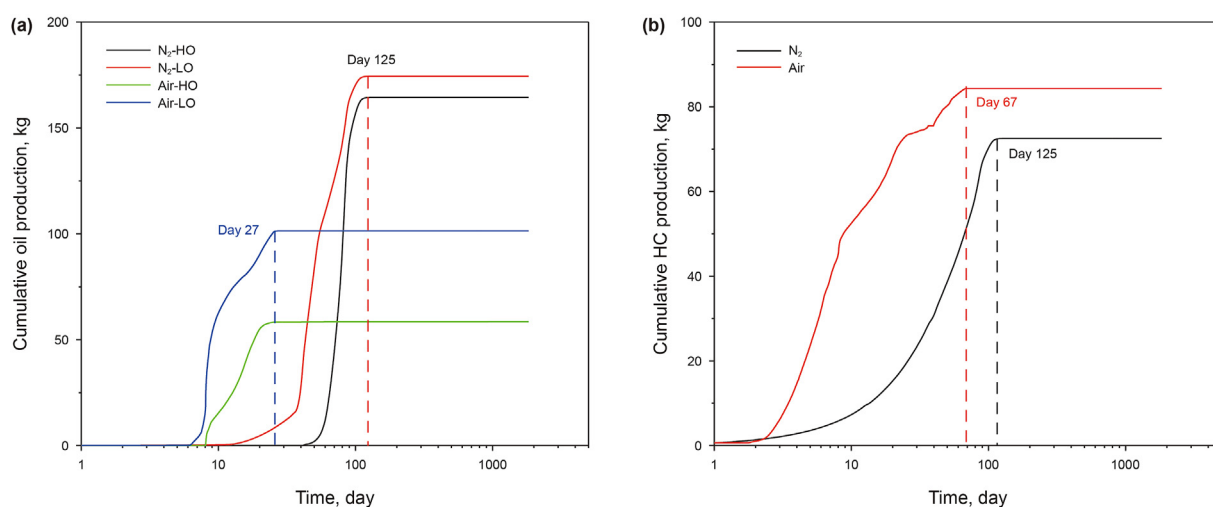

Fig. 6. Cumulative production of oil and gas for the ATS and HNICP: (a) HO and LO; (b) HC.
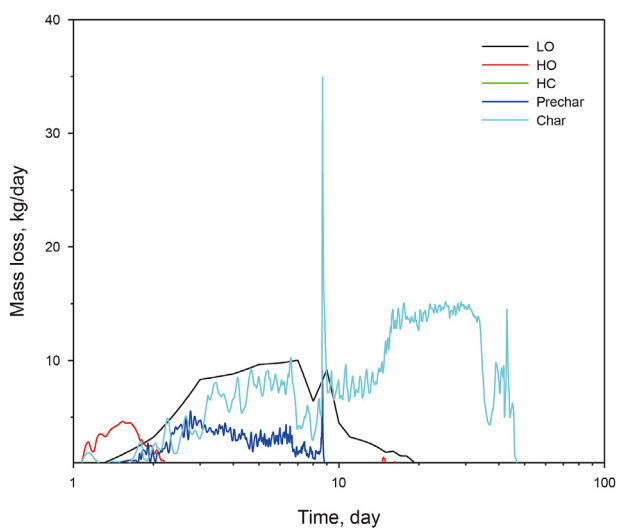

Fig. 7. Mass loss of the oxidation reaction during the ATS.

from the oxidation heat of kerogen pyrolysis residue. Sun et al. (Guo et al., 2020a) found that the oxidation reaction of residual carbon provides the most heat by the elemental analysis. Peng et al., (2013) found the difference in oil recovery between the aerobic and anaerobic retorting processing was small. However, the above experiments all used packing oil shale particles, which did not consider overburden pressure and heat loss. Wang et al., (2018) found the calorific value of kerogen pyrolysis residue is about 35% of the total calorific value of oil shale. Although there is a mass of oxidation heat with kerogen pyrolysis residue during ATS, a large proportion of heat was lost in the fluid phase change and outside of the target area. Zhang et al. (Zheng et al., 2017) found the effect of injection rate and oil content of gas on the movement of the temperature front was important. Except for the laboratory experiment and numerical simulation, an oil shale ATS pilot project was conducted in Songliao Basin, China in 2016, aimed at technical preparation for commercial oil shale ATS production (Bai et al., 2017). However, the output of the production well was very unstable, producing 1.68 tons of oil in three months. By analyzing production data of the oil shale ATS pilot project, Guo et al., (2020b) believed that bad sealing of the formation led to the low oil recovery. Although the feasibility of ATS has been verified by the pilot project,
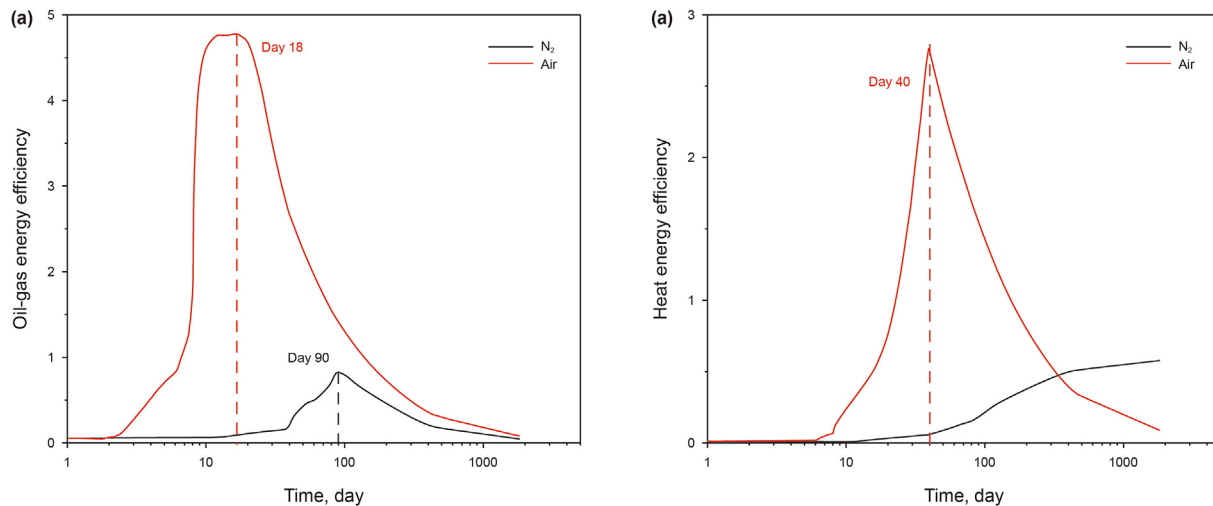
Fig. 8. Energy efficiency for the ATS and HNICP: (a) Oil-gas energy efficiency; (b) Heat energy efficiency.

its energy efficiency failed to achieve the lower limit of oil shale economic development. The heating mechanism and the characteristic of different reaction zones are still unclear.

In this study, an ATS numerical simulation model was proposed for the development of oil shale, which considers the pyrolysis of kerogen, high-temperature oxidation, and low-temperature oxidation. The evolution of oil, O_2, and solid organic matter distribution was analyzed during the ATS. The effect of preheating temperature, O_2 content, and injection rate on recovery factor and energy efficiency were studied by the model. Finally, the optimal compatibility between O_2 content and injection rate was obtained.

2. Numerical simulation study

2.1. Numerical simulation model and well constraints

CMG STARS™ is a mature commercial compositional thermal simulator, which was used for the simulation of the ATS for oil shale recovery. A typical hexagon well pattern, including one injector and two producer, was adopted for oil shale ICP. As shown in Fig. 1, only one-sixth of the well pattern was considered in this study. Because of the tightness of the oil shale formation, the ATS had to be combined with fracturing technology, and the oil shale formation was considered a dual permeability system (Fig. 1). Because the bedding is widespread in the oil shale formation, there is a larger amount of microcrack in the shale formation after the hydro-fracturing. Therefore, all the fracture space in the three directions was assumed to be 0.1 m. The depth, thickness, and well space of the formation were assumed to be 500, 0.1, and 10 m, respectively. The geological model was set as a regular Cartesian grid, which uses the finite difference discretization method. Because the local violent transformation of matter and energy during ATS decreased the convergence of this model (Li et al., 2015), a small uniform grid size (0.1732 m × 0.1 m × 0.1 m) was used in this model with a grid number of 5151.

Heat loss was neglected in this modeling (Fan et al., 2010) because the effect of heat loss on the ICP is closely related to the thickness of the oil shale. The thicker the oil shale, the smaller the effect of heat loss, which is not the focus of this study. The injection well was constrained by a constant gas injection rate with a constant temperature and a constraint condition (bottom hole pressure <20 MPa). The production wells were constrained by a constant bottom hole pressure of 200 kPa.

There are kerogen and pores in the oil shale, except for the inorganic matter (Zhu et al., 2019). The relationship between the concentration of kerogen and porosity is easy to be obtained by volume conservation. The density of the oil shale is calculated by Eq. (1).

$$\rho_t = \rho_{in} - \varphi_{oe}\rho_{in} + \varphi_k(\rho_k - \rho_{in}) \tag{1}$$

The mass of organic matter in shale can be calculated by Eq. (2) according to the Rock-Eval pyrolysis theory (Langford and Blanc-Valleron, 1990).

$$m_k = m_k^i m_t = \frac{TOC}{\gamma_C}m_t \tag{2}$$

The porosity of kerogen in the shale is calculated by Eq. (3).

$$\varphi_k = \frac{V_k}{V_t} = \frac{m_k\rho_t}{m_t\rho_k} = \frac{TOC}{\gamma_C}(1 - \varphi_{oe}) \tag{3}$$

Finally, the concentration of kerogen in the pore can be calculated by Eq. (4).

$$C_k = \frac{1000m_k'\rho_t}{M_k\varphi} = \frac{TOC}{\gamma_C}\frac{1000\rho_t}{M_k\varphi} = \frac{1000}{M_k(\frac{\gamma_C\varphi_{oe}}{TOC\rho_t} + \frac{1}{\rho_k})} \tag{4}$$

In this study, high-quality oil shale from the Songliao Basin of China was chosen as the research objective (He et al., 2021b; Tong et al., 2011). The original effective porosity for matrix and average TOC were assumed to be 6.40% and 16.9%, respectively. The effective pore space was initially 100% filled with water. The thermal conductivity and heat capacity of matrix rock were assumed to be 1.21×10^5 J/(m day °C) and 1.50×10^6 J/(m³ °C), respectively (Wang et al., 2018a). The mass fraction of C and the molecular weight of kerogen were assumed to be 0.71 and 14.7 g/mol, respectively. According to Eqs. (1)–(4), the porosity of kerogen in the shale and the concentration of kerogen in the pore were 22.2% and 6.34×10^4 mol/m³. Therefore, the total porosity for the matrix is 28.65% in this study. The physical characteristics of the shale are shown in Table 1.

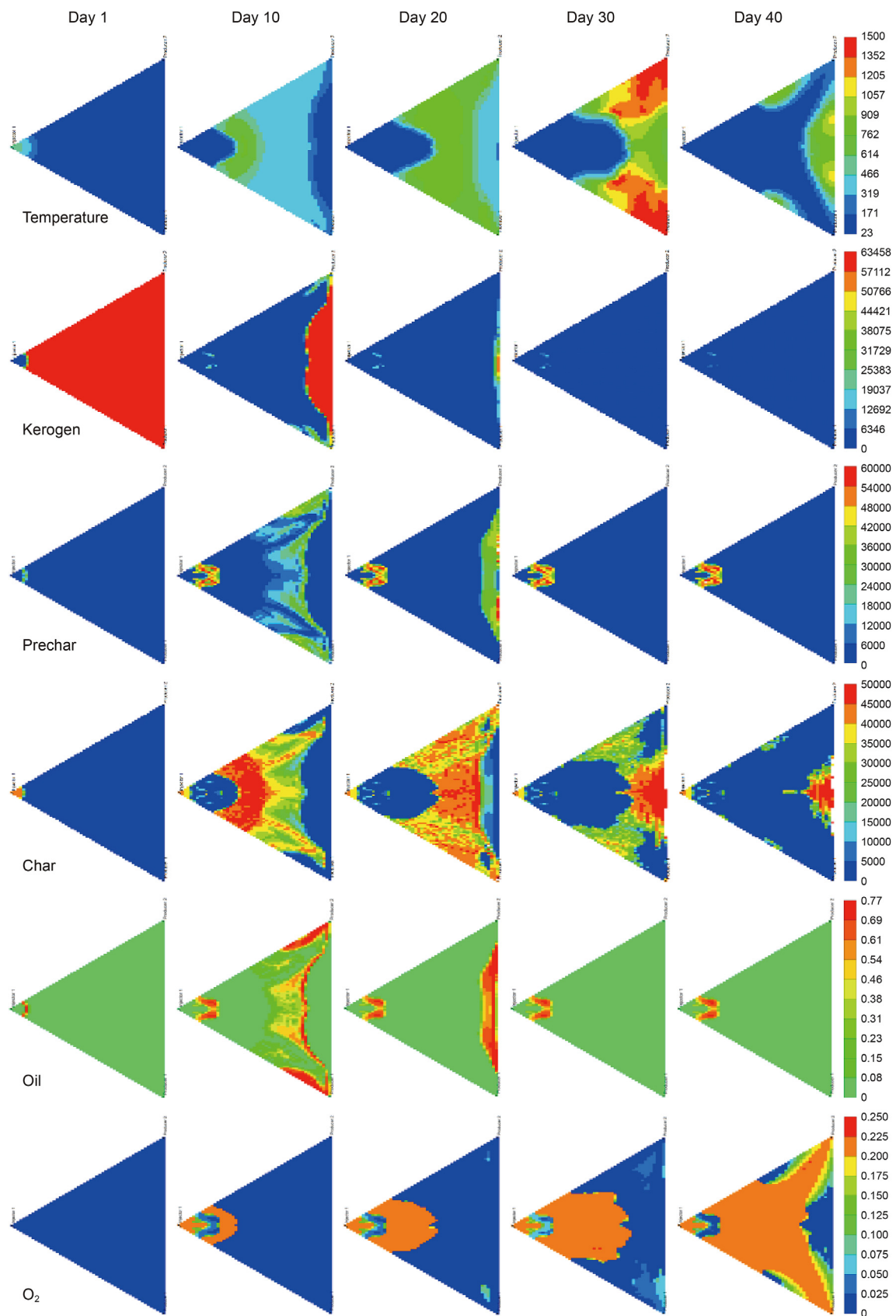**Fig. 9.** Temperature, O_2, and organic matter content distribution in the matrix during the ATS.
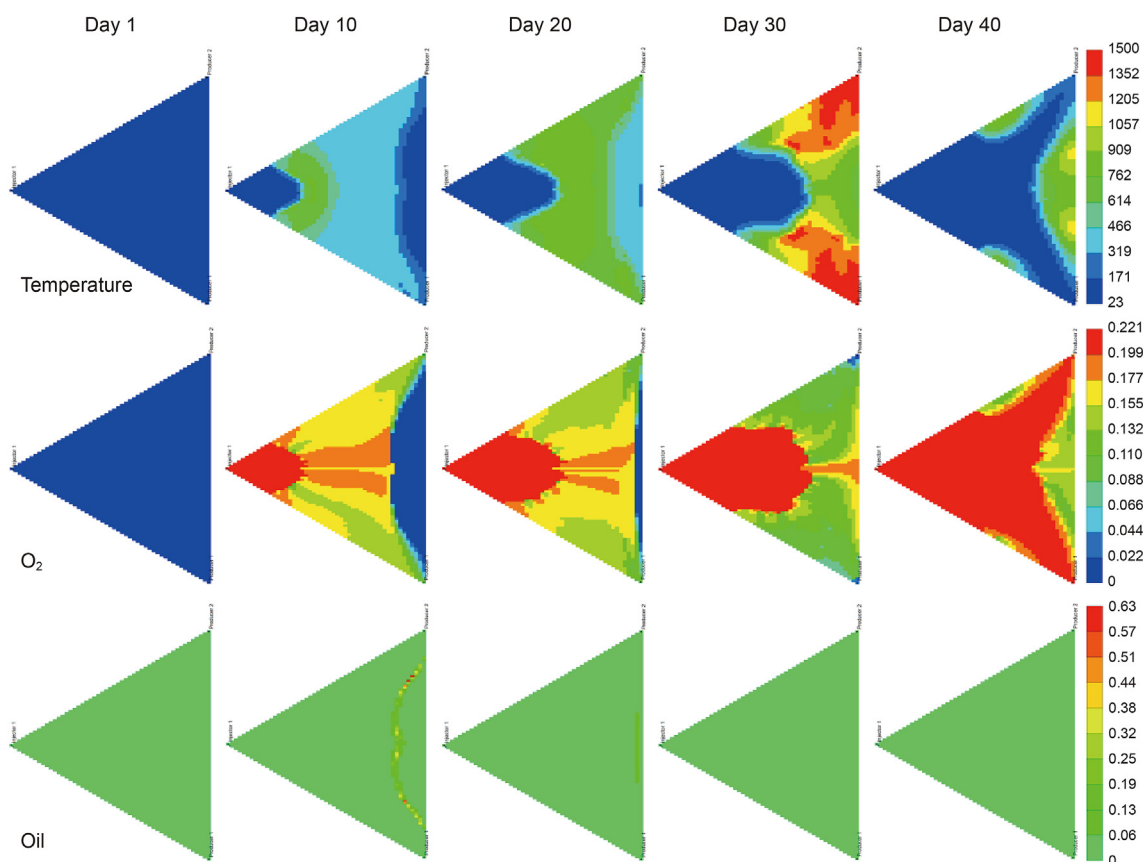
Fig. 10. Temperature, O_2, and oil distribution in the fracture during the ATS.
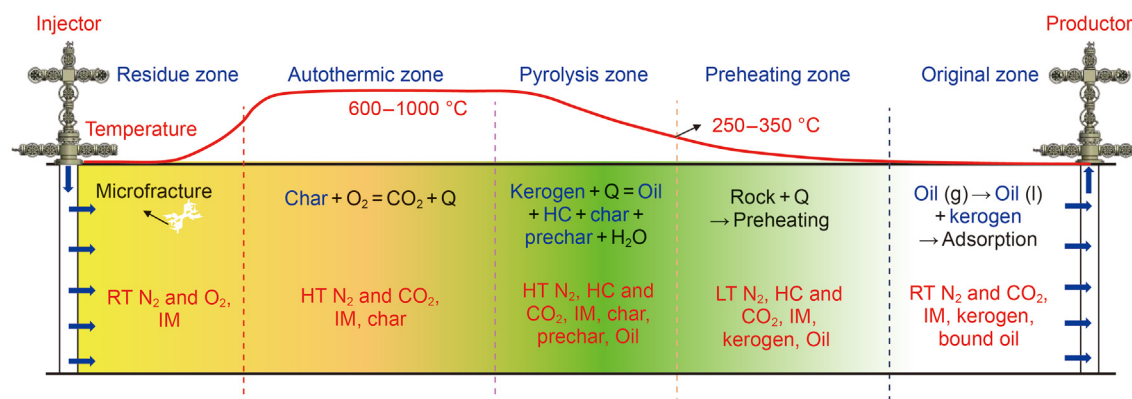

Fig. 11. Five characteristic zones for the ATS.

2.2. Reaction models for pyrolysis and oxidation of organic components

The chemical reaction during the autothermic pyrolysis in-situ conversion process mainly includes two main parts: pyrolysis and oxidation of organic components, which are controlled by the temperature and oxygen content. The oxidation reaction of organic components happens with higher oxygen content. On the contrary, the pyrolysis of organic components happens with lower oxygen content. According to the previous study, the pyrolysis and oxidation reactions were multi-stage parallel reaction models, which included 4−6 simple reactions. To describe the different reactions, three sets of parameters should be provided: reaction equation, frequency factor and activation energy, reaction enthalpy, which

describe the conversion of organic components, reaction speed, and the change of heat, respectively.

The Braun and Burnham model (BB model) (Braun and Burnham, 1992) was commonly used to describe the pyrolysis of oil shale, which has been verified by a large number of laboratory experiments. To simplify and improve computability, the BB model was modified by Pei (Pei et al., 2018), which included six pseudo components and four reactions. The six pseudo components include kerogen, heavy oil (HO), light oil (LO), hydrocarbon gas (HC), prechar, and char. This simplicity may cause less HC gas production and more coke generation than the original Braun and Burnham model. But the simulation results showed this impact can be ignorable. This simplification may also cause faster heat transfer and more active chemical reactions (Pei et al., 2018). However, this
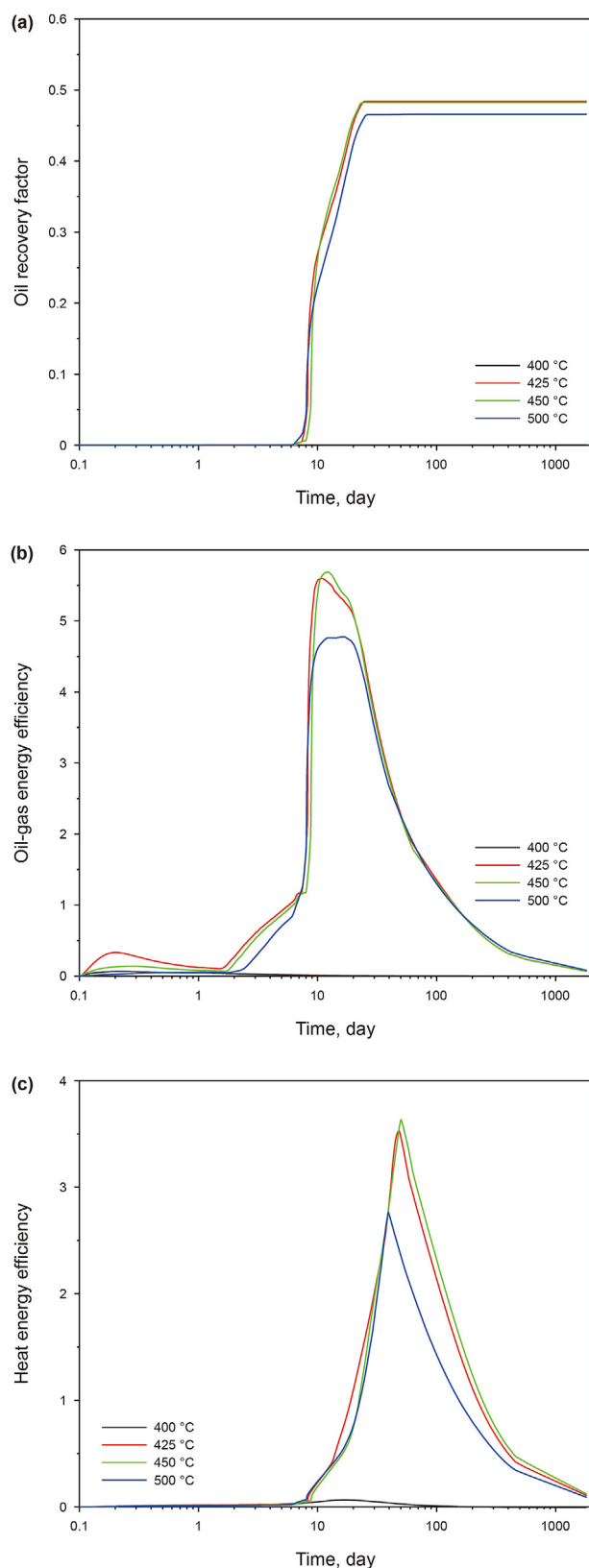
Fig. 12. Oil recovery factor and energy efficiency for different preheating temperatures during the ATS: (a) Oil RF; (b) Oil-gas energy efficiency; (c) Heat energy efficiency.

composition of oil and gas obtained from the oil shale from Songliao Basin (He et al. 2019, 2021a). Therefore, similar pseudo components and molecular weight were used in this study. The molecular weight of kerogen is tested by the organic element analysis.

Because the pyrolysis and oxidation reaction of organic components in this study was provided by different studies (Braun and Burnham, 1992; Khakimova et al., 2019; Pei et al., 2018; Sun et al., 2015a), the relevance of pyrolysis and oxidation reaction from different studies was bad. Therefore, elements of conservation were used to modify the coefficient of chemical reactions. Therefore, molecular formulas are necessary for this study. If the HO, LO, and HC were assumed to be saturated hydrocarbon, the molecular formulas of HO, LO and HC were also obtained, which are shown in Table 2. According to the molecular formula and elements of conservation, the coefficients of reactions 1–4 were modified, which were shown in Table 3. The modified BB model includes pyrolysis of kerogen, pyrolysis of HO, pyrolysis of LO, and pyrolysis of prechar. The frequency factor, activation energy, and reaction enthalpy of reactions 1–4 were provided by Braun and Burnham (Braun and Burnham, 1992; Lee et al., 2018), which have been used in a field pilot simulation in Colorado Green River with a hexagonal well pattern of the Shell electrical heating technology (Fowler and Vinegar, 2009; Pei et al., 2018). Because the kerogen type and sedimentary environment of Songliao Basin are similar to the Green River oil shale, which are type I-II and lacustrine shales, the kinetic parameters of Green River oil shale are applied in the Songliao Basin oil shale.

The oxidation reactions of the organic component are more complex than the pyrolysis reactions, which have been studied by Khakimova (Khakimova et al., 2019). In the study, the oxidation reactions of the organic component were divided into low-temperature oxidation reactions and high-temperature oxidation reactions. The low-temperature oxidation reactions are comprised of the oxygen-addition reaction of kerogen and bond scission reaction of LO and HC, which happens lower than 350 °C. The high-temperature oxidation reaction is the bond scission reaction of HO and non-generative organic, which is prechar and char in this study. The reaction products of the bond scission reaction are water and IG, which consists of 80% carbon dioxide and 20% carbon monoxide. To be consistent with the pyrolysis reaction, the Khakimova model is simplified and modified. First, the source of the oil shale is unavailable in Khakimova's study. Although the molar weight of organic components was provided, it is different from the BB model, which may be caused by the partition criterion difference of organic components. However, to ensure relevance and consistency for all the reactions, the molar weight of organic components in the BB model was used in this study. Therefore, the stoichiometric coefficients of reactions 5–10 were obtained easily by the molecular formula and elements conservation, which are shown as reactions 5–10 in Table 3.

Second, because the molar weight of organic components of Khakimova's study was not used in this study, the frequency factor, activation energy, and reaction enthalpy in Khakimova's study are also inapplicable for reactions 5–10. The kinetic study of Songliao Basin oil shale oxidation was studied by Sun et al. (2015a). Multi-stage parallel reaction model and bi-Gaussian distribution function were introduced to analyze the overlapping peaks in DTG. The frequency factor and activation energy for a four-stage parallel reaction was estimated using the Coats and Redfern, FWO, and Star-ink methods, and Malek's method to characterize the oxidation process of organic components in oil shale. Because the physical properties of LO and HC, prechar, and char are similar separately (Braun et al., 1984; Yuan et al., 2018), the frequency factor and activation energy of reactions 6 and 7, and reactions 9 and 10 in the
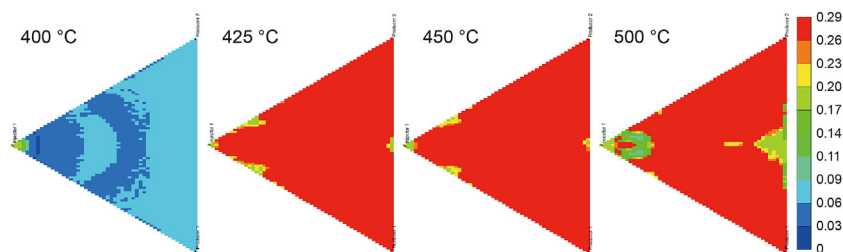
impact was very small relative to the heat input via the heating process (Fan et al., 2010). The molecular weight of the pseudo components is shown in Table 2, which is similar to the

Fig. 13. Porosity distribution after the ATS for different preheating temperatures.

reaction model used the same value. Because the above kinetic parameters were all tested by DTG with the Songliao Basin oil shale, the reaction speed of reactions 5–10 can be well described.

Because the heat released by oxidation reactions supports the pyrolysis reactions of oil shale, the reaction enthalpy of oxidation reactions is the most important parameter for ATS. Although the total reaction enthalpy is easy to test (Bai et al., 2015; Guo et al., 2020a), it is difficult to obtain the reaction enthalpy of reactions 5–10. The main reason is that the different organic components are difficult to separate. In this study, the reaction enthalpy of reactions 5–10 was calculated by the difference of atomization energy between the reactants and products, as shown in Table 4. The atomization energy of different organic components (Table 4) was calculated by the bond energy of chemical bonds, including C—C (332 kJ mol^{-1}), C—H (332 kJ mol^{-1}), O—H (332 kJ mol^{-1}), O=O (332 kJ mol^{-1}) and C=O (802 kJ mol^{-1}), which is easy to obtain, Luo's study (Luo, 2005). It has been reported that there is only a 2% deviation in atomization energy for saturated hydrocarbons with this method (Skinner and Pilcher, 1963).

The Arrhenius rate constant is commonly used to describe the reaction rate, which can be calculated by Eq. (5).

$$k_{A} = Ae^{-\frac{E}{RT}} \tag{5}$$

The relationship between the Arrhenius rate constant of different reactants and temperatures is shown in Fig. 2. The results show that oxidation of kerogen, LO, and HC began at 250–300 °C, which is much lower than the oxidation of HO, prechar, and char and the pyrolysis of kerogen, HO, LO, and prechar (400–500 °C). Moreover, there is a reaction temperature upper limit for the low-temperature oxidation reaction and high-temperature oxidation reaction (Fan et al., 2015). Therefore, it is necessary to set a reaction temperature upper limit during the simulation. When the temperature is larger than the reaction temperature upper limit, the Arrhenius rate constant was constant. The simulation results showed the reaction temperature upper limit for reactions 1–4, 5–7, and 8–10 are 500, 300, and 550 °C, respectively. The Arrhenius rate constant of oxidation reactions was usually larger than the pyrolysis reactions.

2.3. Seepage characteristic during ATS

Because the temperature and pressure varied considerably during the ATS, the phase state and viscosity of HO and LO changed with temperature and pressure. The phase behavior of LO and HO has been studied in the innovative nitrogen injection assisted small well spacing electric heating study (Pei et al., 2018), which is also been used in this study. The critical pressure of LO and HO are assumed to be 1.79 and 1.07 MPa, respectively. The critical temperature of LO and HO are assumed to be 453.86 and 594.98 °C, respectively. And the acentric fact of LO and HO are assumed to be 0.684 and 1.042, respectively (Pei et al., 2018). According to the PR equation of state (Cismondi and Mollerup, 2005), the pressure-

temperature phase diagram (vapor pressure curve) of LO and HO was calculated, shown in Fig. 3(a). Because the pressure of the production well was 0.2 MPa in this study, the phase inversion temperature for LO and HO was 90–180 and 236–320 °C, respectively. For the oleic phase, the viscosity-temperature relationship of LO and HO is shown in Fig. 3(b), which is obtained by Pei's study (Pei et al., 2018).

As a low maturity shale, 90% of kerogen in oil shale does not translate into oil and gas (Bai et al., 2015). Similar to the shale gas and oil reservoir, the reservoir spaces mainly refer to organic pore, inorganic pore, and fracture (Sang et al., 2018). As a result of the pressure, kerogen strength, and mass loss of solid, the pyrolysis of kerogen and compaction show in an alternant way (Burnham, 2017). Therefore, porosity and permeability can evolve along with the pyrolysis of kerogen, as well as the compaction and expansion of rocks and fluid during the ATS. According to a laboratory experiment (Wang et al., 2019; Li et al., 2016), the permeability increases from 0.01 to 6529.4 mD. According to the results, the variation of permeability with the porosity change can be modeled using the Carmen-Kozeny equations (Cui et al., 2018). In more general terms, the reaction kinetics that dictates the evolution of solids and fluids in pyrolyzing oil shale also control multiphase transport properties in the oil shale (Kibodeaux, 2014). However, there is little evolution of the relative permeability during the in-situ conversion process for oil shale, which is ignored in this study. As shown in Fig. 4, the relative permeability curves for the matrix and fracture of the shale are obtained from the Wolfcamp and Eagle Ford shale samples (Ma, 2015; Ojha et al., 2017).

2.4. Model Validation

In order to verify the reliability of the model, an autothermic pyrolysis laboratory experiment of oil shale using high- and normal-temperature air in sequence as carrier gases, which was conducted by Sun et al. (2015b) with a highly instrumented fixed bed simulating the horizontal stratum, was fitted with the numerical simulation model. The fixed bed consisted of a horizontal cylindrical reactor chamber with an internal diameter of 32.5 cm and a length of 200 cm. Seven temperature sensors were placed separately at 10, 40, 70, 100, 130, 160 and 190 cm to test the temperature evolution of oil shale pyrolysis in porous media. A mass of large oil shale particles (2–100 mm, 110–120 kg), mimicking an anisotropic artificial fracture, was introduced into the fixed bed.

Therefore, a simulation model with 200 cm was built to model the autothermic pyrolysis process. As shown in Fig. 5(a) and (b), the model includes 400 layers in the flow direction. All of the formation parameters have been listed in Table 1. However, because the insulation measure of the highly instrumented fixed bed was rather simple and crude, the heat loss in the radial direction should be considered. The thermal conductivity of the heat loss in the radial direction was obtained by the data fitting, which was 5 × 10^5 J/(m day °C). Because the oil shale particle with 2–100 mm was used as
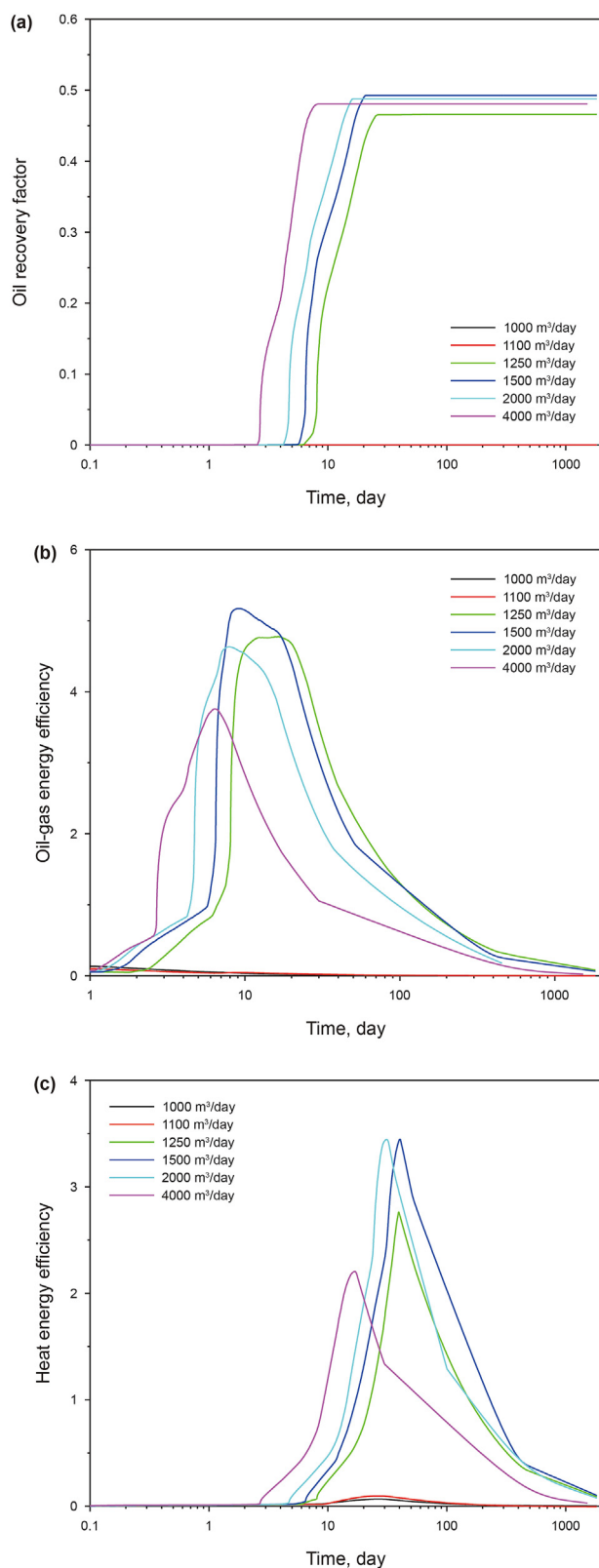
(a)

(b)

(c)

Fig. 14. Oil recovery factor and energy efficiency for different injection rates during the ATS: (a) Oil RF; (b) Oil-gas energy efficiency; (c) Heat energy efficiency.

the sample, 0.05 m was used as the fracture space in this study. According to Sun et al.'s study (Sun et al., 2015b), three autothermic pyrolysis laboratory experiments with different injection time were conducted in the same sample and the continuous oxidation

reaction of oil shale was all successfully implemented for the three experiments. Therefore, only the first autothermic pyrolysis laboratory experiment was used to verify the model. In the first stage, 500 °C heat air was injected into the sample for 30 min with 25 m^3/ h. Then, room temperature air was injected into the sample for 600 min with the same flow. Finally, the air injection was stopped to cool the sample for 900 min. Data fitting of the temperature evolution during the autothermic pyrolysis laboratory experiment was shown in Fig. 5. The calculated results from the numerical simulation model corresponded with the experimental data, which verifies the reliability of this model.

3. Results and discussion

3.1. Mechanism of the ATS

Comparing the ATS and the HNICP, the mechanism and advantage of ATS were studied, based on numerical simulation. For the ATS, 500 °C N$_2$ was injected into the formation with 1250 m^3/day for 1 day. There are two reasons for this operation: a small amount of kerogen near the injector well was thermally pyrolysis into oil, gas, prechar, and char, which provided plenty of oxide for the oxidation reaction; the high temperature also enabled the oxide to reach the trigger temperature of the oxidation reaction. Then, room temperature air (25 °C) was injected into the formation with 1250 m^3/day. As for HNICP, 500 °C N$_2$ was injected steadily into the formation with 1250 m^3/day for 5 years.

The cumulative production of HO, LO, and HC for the ATS and HNICP are shown in Fig. 6. It can be seen that the cumulative HO and LO production of the ATS was 58.14 and 101.24 kg, which is smaller than that of the HNICP (164.25 and 173.81 kg). There are two reasons for this phenomenon. According to the temperature distribution in Fig. 9, the pyrolysis temperature during the ATS was generally larger than 500 °C, which is the pyrolysis temperature of HNICP. Therefore, the secondary thermal pyrolysis of HO and LO (reactions 2–3) during the ATS was stronger than the HNICP. A great deal of HO and LO were converted to HC. As shown in Fig. 6(b), the cumulative production of HC for the ATS (83.99 kg) was larger than that for the HNICP (72.34 kg). Part of the HO and LO was oxidized (reactions 6, 8) during the ATS. The mass loss of HO, LO, HC, prechar, and char during the ATS, which was caused by oxidation, is shown in Fig. 7. The results showed that 89.91 kg LO and 7.20 kg HO were oxidized during the ATS. If the total cumulative oil production of HNICP was used as a benchmark, 47.15% of the oil was produced from the production well and 28.73% of the oil was oxidized during the ATS. The remaining 24.12% oil was secondary thermal cracked. Although a larger amount of oil was oxidized during the ATS, little of the HC was oxidized, according to Fig. 7. The results show that better fluidity of HC can avoid the meeting of HC and O$_2$. The production time of ATS lasted for 67 days, which was much less than that of HNICP (125 days). The reason for this was that the intense heat, which is caused by the oxidation reaction, ensures the system reaction speed. At the same time, the loss of prechar and char increased the porosity and permeability of the matrix of the formation, which is good for convective heat transfer and oil-gas production.

The injection energy during the ATS includes the heat capacity of the injected gas and the energy of the gas compressor during the isothermal compression process. The production energy during the ATS includes the calorific of oil-gas and the residual heat capacity of production gas. The oil-gas energy efficiency and heat energy efficiency are calculated, respectively.

The power of the gas compressor during the isothermal compression process, in which the gas is usually assumed as an ideal gas, can be calculated as follows:
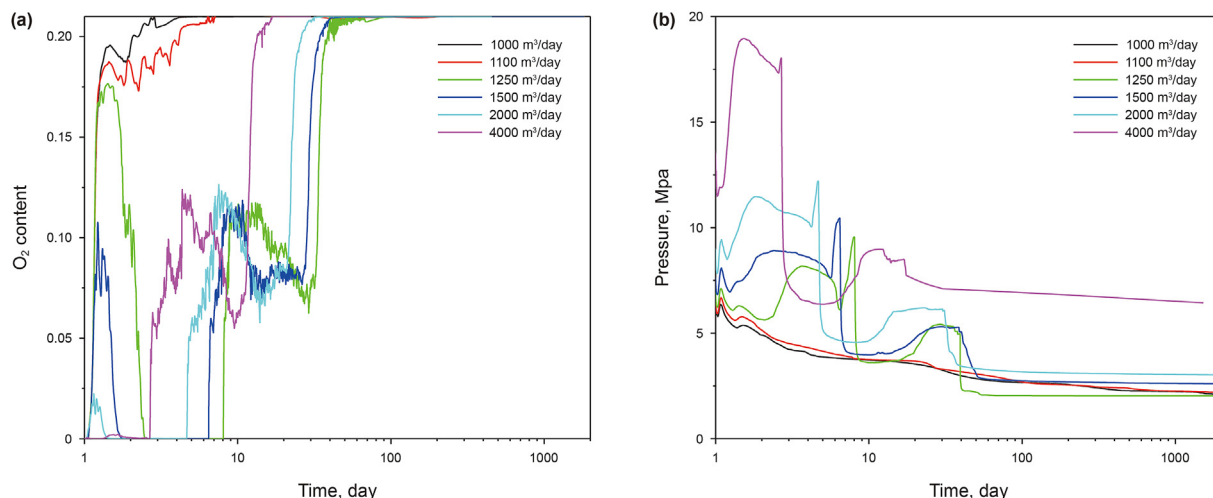
Fig. 15. O_2 content of the production well and pressure of the injection well for different injection rates during the ATS: (a) O_2 content of the production well; (b) Pressure of the injection well.

$$N_c = 10^3 \times p_{sc} q \ln \frac{p_{in}}{p_{sc}} \tag{6}$$

The heat power of gas can be calculated by Eq. (7).

$$N_h = cq\rho\Delta T \tag{7}$$

Therefore, the oil-gas energy efficiency and heat energy efficiency are easily obtained by Eq. (8).

$$\begin{cases} f_{og} = \dfrac{\sum\limits_{t=0}^{n} N_{og}}{\sum\limits_{t=0}^{n} N_c + \sum\limits_{t=0}^{n} N_h^{in}} \\[4ex] f_h = \dfrac{\sum\limits_{t=0}^{n} N_h^{out}}{\sum\limits_{t=0}^{n} N_c + \sum\limits_{t=0}^{n} N_h^{in}} \end{cases} \tag{8}$$

The calorific of oil and gas (Wang et al., 2018b) is assumed to be 40.0×10^6 and 35.6×10^3 J/m^3, respectively.

As shown in Fig. 8, the energy efficiency for the ATS and HNICP were calculated according to Eqs. (6)–(8). The energy efficiency, both oil-gas and heat, of ATS was much larger than the HNICP. The maximum oil-gas energy efficiency of ATS was 4.79, which was 5.84 times that of HNICP (0.82). The max heat energy efficiency of ATS was 2.75, which was 4.74 times that of HNICP (0.58). For ATS, there is only a one-day high temperature nitrogen injection to provoke the oxidation reaction. Most of the energy consumption comes only from isothermal compression energy. Therefore, the energy efficiency of ATS is much larger than that of HNICP. Another advantage of ATS is that the energy contained in residual organic matter (prechar and char) is also developed in the form of heat, in addition to providing the enthalpy of pyrolysis reaction. In 27 days, the temperature of production well gas was higher than 300 °C and the maximum heat power of the gas products reached 6.85×10^3 J/s. The time of maximum oil-gas energy efficiency of HNICP (day 18) and of ATS (day 90) was less than the production time of oil-gas, which was day 67 and day 125, respectively. The results indicate that in the production tail, the low production rate cannot cover the

energy consumption for ATS, and there is an optimal production cycle, which should consider the previous investment.

The temperature and organic matter content distribution in the matrix during the ATS are shown in Fig. 9. It can be seen that the oxygen content of the gas phase near the injector well is the largest, followed by char, prechar, and kerogen in the direction of percolation flow. The boundary between oxygen and char served as the place for oxidation reaction, which has the maximum temperature. The temperature in the boundary between prechar and kerogen was about 350 °C, which served as the end for pyrolysis reaction. The oil was distributed mainly over prechar. There was little O_2 near the oil zone in the matrix, which indicated that oxidation of oil during the ATS mainly occurred within the fracture. The temperature, O_2, and oil distribution in the fracture during the ATS were shown in Fig. 10. The oil had direct contact with O_2, which led to high temperature in the fracture at 30 day near the productor.

According to the temperature, O_2, and organic matter content distribution, the formation during the ATS can be divided into five characteristic zones, as shown in Fig. 11, including residue zone, autothermic zone, pyrolysis zone, preheating zone, and original zone. For the residue zone, there is only room temperature (RT) N_2, O_2, and inorganic matter (IM) in the matrix. The oxidation reaction of char occurred in the autothermic zone, which included high temperature (HT) N_2, CO_2, IM, and char. The pyrolysis of kerogen occurred in the pyrolysis zone, which included HT N_2, HC, CO_2, IM, char, prechar, and oil. The temperature of preheating zone was lower than 350 °C, including low temperature (LT) N_2, HC, CO_2, IM, kerogen, and oil. Because the temperature of the original zone decreased to RT, part of the oil changed from the gas phase to the liquid phase, which will be adsorbed in the kerogen. All of the five characteristic zones keep moving during the ATS, which ensures continuous production of heat, oil, and gas.

3.2. Effect of preheating temperature

The preheating temperature is an important parameter during the ATS, which affects the heat energy of injection gas and the evolution of the temperature field. Therefore, the ATS with different preheating temperatures (400, 425, 450, 500 °C) was studied in this section.

The oil recovery factor and energy efficiency for different preheating temperatures during the ATS are shown in Fig. 12. To
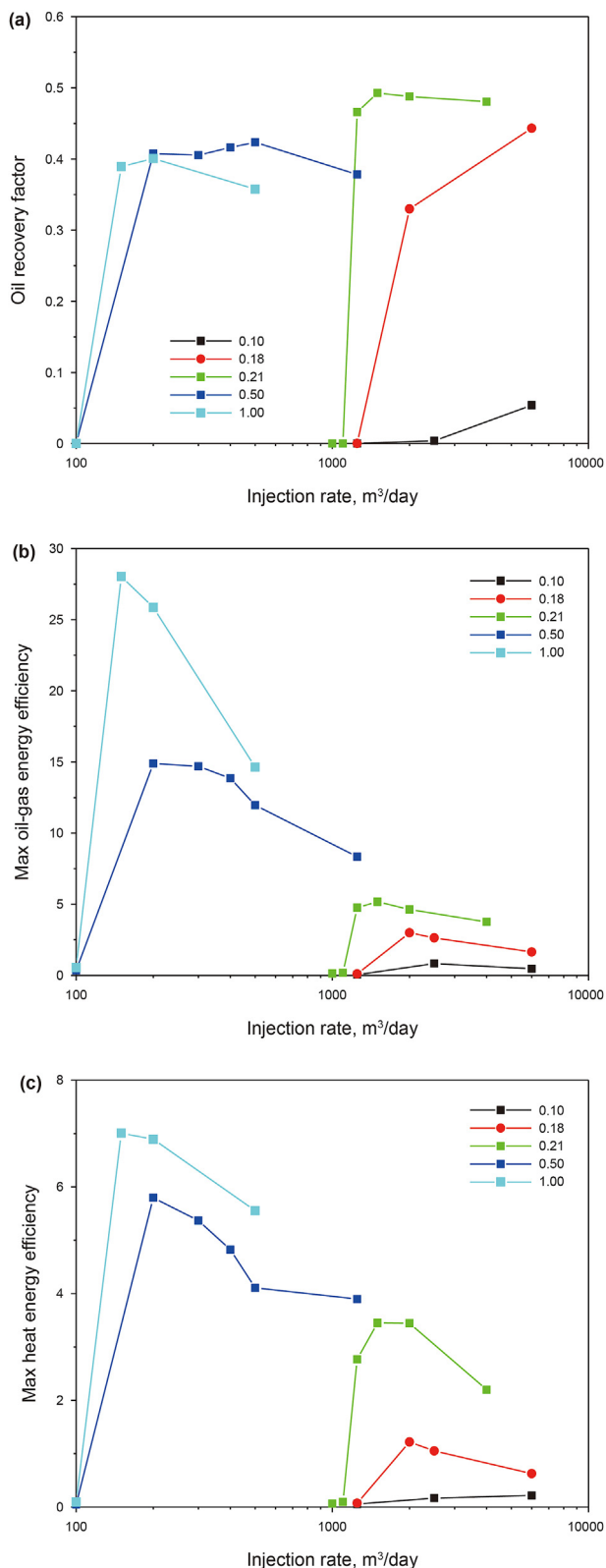
Fig. 16. The effect of O_2 content and injection rates during the ATS: (a) Oil recovery factor; (b) Maximum oil-gas energy efficiency; (c) Maximum heat energy efficiency.

preheating temperature increased to 425 °C, the ATS was built and the oil RF reached 48.75%. The oil RF slightly decreased with the increase in temperature. When the preheating temperature increased from 425 to 500 °C, the oil RF decreased by 2.09%. For energy efficiency, the maximum oil-gas energy efficiency decreased from 5.613 to 4.776 and the maximum heat energy efficiency decreased from 3.528 to 2.770 when the preheating temperature increased from 425 to 500 °C.

This can be explained by porosity distribution after the ATS for different preheating temperatures in Fig. 13. The results showed that when the high-temperature N_2 was changed to room temperature air within a short time, the zones near the injection well were rapidly cooled. Therefore, a small amount of prechar and char was not oxidized and there was a low porosity zone near the injection well. The pyrolysis area gradually increased with the preheating temperature increasing on the first day, which produced more prechar and char. The low porosity zone near the injection well increased with the preheating temperatures during the ATS. In this zone, a small amount of oil was bound, and part of prechar and char was not oxidized, which led to low oil RF and heat production. A high preheating temperature increased the heat energy injection at the preheating stage. The energy efficiency decreased with the increase of high preheating temperature during the ATS.

3.3. Effect of O_2 content and injection rate

The O_2 content and injection rate control the injection rate of O_2 and N_2 during the ATS, which determines the heat intensity of organic matter oxidation and convective heat transfer efficiency. The effect of air injection rate on the ATS was studied, including 1000, 1100, 1250, 1500, 2000, and 4000 m^3/day.

The oil recovery factor and energy efficiency for different injection rates during the ATS are shown in Fig. 14. It can be seen that when the injection rate of air was less than 1100 m^3/day, a continuous autothermic pyrolysis reaction cannot be triggered. According to Fig. 15(a), O_2 content was down at the beginning for 1000 and 1100 m^3/day. However, because of the low O_2 injection rate, the formation does not have enough heat in it to support the oxidizing reaction temperature. The result indicates that there is an injection rate threshold with the same oil content for the autothermic pyrolysis reaction. When the injection rate of air was larger than 1250 m^3/day, the oil recovery factor and maximum energy efficiency were raised at the beginning (1250−1500 m^3/day) and then declined (1500−4000 m^3/day) with the injection rate of air. According to Fig. 15(a), when the injection rate of air is just over the threshold, there is a higher O_2 content in the production well at the beginning, which indicates that part of the prechar and char near the injection well was not oxidized, as shown in Fig. 13. Therefore, the production of oil and heat decreased, which led to a lower oil recovery factor, oil-gas energy efficiency, and heat energy efficiency. The increasing injection rate caused a higher injection pressure, Fig. 15(b), which increased the energy injection of an isothermal compression. As a result, the oil-gas energy efficiency and heat energy efficiency were both greatly reduced when the injection rate increased from 1500 to 4000 m^3/day.

The injection rate threshold for different O_2 content (0.1, 0.18, 0.21, 0.5, 1) was studied to find the cooperative relationship between the O_2 content and injection rate during the ATS. The effect of injection rates on oil recovery factor and maximum energy efficiency for different O_2 content during the ATS is shown in Fig. 16. When the O_2 content was larger than 0.18, the oil recovery factor decreased with an increase of O_2 content. The reason for this is that the excess O_2 in the oil shale formation leads to an increase of oil oxidation in the fracture. The porosity distribution after the ATS for different O_2 content was shown in Fig. 17, and a larger amount of

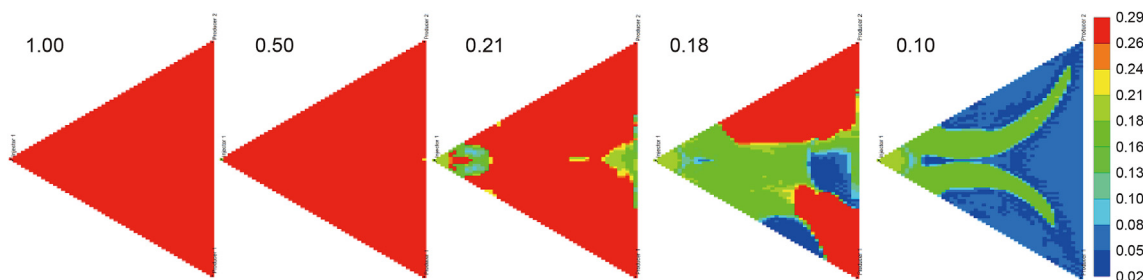compare with the HNICP, it was assumed that the cumulative production of oil for the HNICP (338.06 kg) was the total oil in the formation. It can be seen that the oxidation reaction was not triggered at 400 °C and there is almost no oil production. When the

Fig. 17. Porosity distribution after the ATS for different O_2 content.
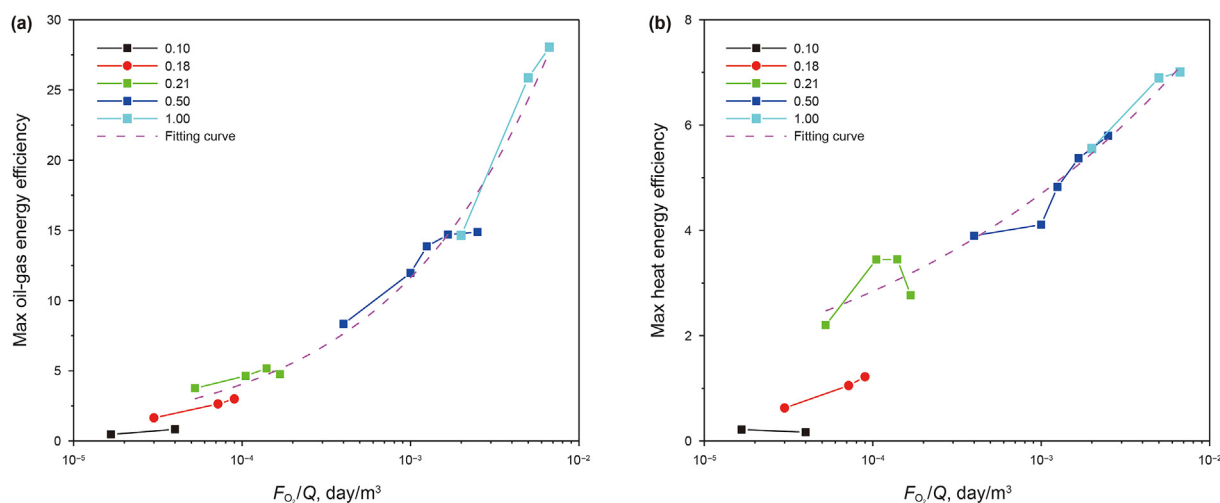

Fig. 18. Relationship between the energy efficiency and F_{O2}/Q: (a) Maximum oil-gas energy efficiency; (b) Maximum heat energy efficiency.

Table 1
Physical characteristics of the shale.

Parameter	Value
Original formation pressure, kPa	4500
Original formation temperature, °C	35
Total porosity for matrix, %	28.65
Original effective porosity for matrix, %	6.40
Matrix permeability, mD	0.01
Fracture permeability, mD	100
Initial fluid saturation in matrix and fracture	100% water
Density of matrix, kg/m³	2019.84
Concentration of kerogen in the pore, mol/m³	6.34×10^4
Average total organic carbon content, %	16.9
Thermal conductivity of matrix rock, J/(m day °C)	1.21×10^5
Heat capacity of matrix rock, J/(m³ °C)	1.50×10^6

formation was not swept when the O_2 content was smaller than 0.18. Therefore, the oil recovery factor increased with an increase of O_2 content when the O_2 content was smaller than 0.18. When the O_2 content increased from 0.18 to 1, the injection rate threshold decreased from 2000 to 150 m³/day, which indicates that the lower the O_2 content, the larger the injection rate threshold. Because of the low permeability of the oil shale formation, the injectivity of the injection well is finite. Although 6000 m³/day of gas with 10% O_2

was injected into the formation, the autothermic pyrolysis reaction was not triggered. As for energy efficiency, when the O_2 content increased from 0.18 to 1, the maximum oil-gas energy efficiency decreased from 28.0 to 3.0, and the maximum heat energy efficiency decreased from 7.0 to 1.2. For the autothermic pyrolysis in-situ conversion technology, the enthalpy of the pyrolysis reaction comes from the self-oxidation reaction and the main external energy is isothermal compression energy for the high-pressure gas. Therefore, when the injection rate and pressure sharply decreased, which was caused by the O_2 content increasing, the energy efficiency of the ATS significantly increased. The energy efficiency, both oil-gas and heat, increased with the O_2 content for the same gas flow during the ATS. There are two reasons for this phenomenon: First, the larger O_2 content increased the oxidation reaction rate, which decreased the development time of the ATS. Therefore, the isothermal compression energy for the ATS with high O_2 content gas injection was low. Second, the low O_2 content gas injection (<0.21) caused anisotropy of the ATS, which led to part of the kerogen, prechar, and char not being swept (Fig. 17). Therefore, the total production of oil and heat was larger during the ATS with high O_2 content gas injection.

The O_2 content and the injection rate of gas determine the heat intensity of organic matter oxidation and convective heat transfer

Table 2
Molecular formula and molecular weight of the pseudo component.

Pseudo component	Kerogen	HO	LO	HC	Prechar	Char
Molecular formula	$CH_{1.45}O_{0.04}N_{0.02}S_{0.01}$	$C_{27.17}H_{56.34}$	$C_{15.26}H_{32.52}$	$C_{3.16}H_{8.33}$	–	C
Phase state	Solid phase	Oil phase	Oil phase	Gas phase	Solid phase	Solid phase
Molecular weight, g/mol	14.7	382.4	215.7	46.3	12.7	12.0

Table 3
Reaction models for pyrolysis and oxidation of organic component.

No.	Description	Reactions	Frequency factor, 1/s	Activation energy, kJ/mol	Reaction enthalpy, kJ/mol
1	Pyrolysis of kerogen	Kerogen = 0.0107 HO + 0.0097 LO + 0.0071 HC + 0.6411 prechar	3.0×10^{13}	213.50	−4.20
2	Pyrolysis of HO	HO = 0.6613 LO + 1.5048 HC + 13.4175 prechar	1.0×10^{13}	226.09	−46.50
3	Pyrolysis of LO	LO = 3.2378 HC + 5.1822 prechar	5.0×10^{11}	226.09	−46.50
4	Pyrolysis of prechar	Prechar = 0.01718 HC + 0.9902 char	1.0×10^{13}	226.09	−46.50
5	Oxidation of kerogen	Kerogen + 0.1052 O_2 = 1.4225 prechar	6.47×10^{4}	64.32	27.89
6	Oxidation of LO	LO + 21.864 O_2 = 16.26 H_2O + 15.26 IG	2.61×10^{5}	72.68	7794.69
7	Oxidation of HC	HC + 4.9265 O_2 = 4.165 H_2O + 3.16I G	2.61×10^{5}	72.68	1758.46
8	Oxidation of HO	HO + 38.538 O_2 = 28.17 H_2O + 27.17 IG	2.57×10^{7}	118.44	13735.40
9	Oxidation of prechar	Prechar + 1.1723 O_2 = 0.575 H_2O + 0.9769 IG	6.02×10^{8}	133.91	454.84
10	Oxidation of char	Char +0.9 O_2 = IG	6.02×10^{8}	133.91	315.80

Table 4
Atomization energy of organic components.

Molecular formula	$CH_{1.45}O_{0.04}N_{0.02}S_{0.01}$	$C_{27.17}H_{56.34}$	$C_{15.26}H_{32.52}$	$C_{3.16}H_{8.33}$	Prechar	C
Atomization energy, kJ/mol	619	32,013	18,198	4166	890	664

Table 5
Fitting parameters.

Fitting parameters	a_1	b_1	a_2	b_2
Value	276.19	0.46	2.02	3.09×10^{-5}

efficiency. The external energy-isothermal compression energy is controlled by the injection rate of gas. Therefore, an allometric equation was used to describe the relationship between the ratio of oil content and injection rate and energy efficiency, as shown in Eq. (9).

$$\begin{cases} f_{\text{og}} = a_1 \left(\dfrac{F_{O_2}}{Q} \right)^{b_1} \\ f_{\text{h}} = a_2 \left(\dfrac{F_{O_2}}{Q} \right)^{b_2} \end{cases} \tag{9}$$

The relationship between the energy efficiency and F_{O_2}/Q is shown in Fig. 18. It should be noted that a larger amount of organic matter was not oxidized for the gas injection with low O_2 content (0.18 and 0.1). Therefore, only the gas injection with high O_2 content (0.21, 0.5, and 1) was fitted with Eq. (9). As shown in Fig. 18, Eq. (9) matched the maximum energy efficiency very well and the R^2 was 0.9790 and 0.9558, respectively. The fitting parameters are shown in Table 5. This empirical formula provided a new insight for the energy efficiency prediction of oil shale ATS.

4. Conclusions

An ATS numerical simulation model was proposed for the development of oil shale, which considers the pyrolysis of kerogen, high-temperature oxidation, and low-temperature oxidation. The mechanism of the ATS was analyzed by the evolution of the oil and O_2 distribution, and the solid organic matter. The effect of preheating temperature, O_2 content, and injection rate on the recovery factor and energy efficiency were studied during the ATS. The major conclusions of this study are summarized as follows:

(1) The ATS in the formation can be divided into five characteristic zones: residue zone, autothermic zone, pyrolysis zone, preheating zone, and original zone. The autothermic zone provided plenty of heat for the pyrolysis zone.

(2) The energy efficiency of both oil-gas and heat during the ATS were much larger than the HNICP. However, because of the

oxidation of oil and gas in the fracture, the oil production of the ATS was much less than that of the HNICP.

(3) There is a threshold value of the preheating temperature during the ATS, which is 400 °C in this study. The maximum oil-gas energy efficiency decreased from 5.613 to 4.776 and the maximum heat energy efficiency decreased from 3.528 to 2.770 when the preheating temperature increased from 425 to 500 °C.

(4) There is a threshold value of the oil content and injection rate during the ATS, which is 0.18 and 1100 m^3/day, respectively. Energy efficiency increased with an increase in O_2 content, and it increased with a decrease in injection rate. The optimal compatibility relationship between energy efficiency and the ratio of oil content and injection rate can be described by the allometric equation.

References

Aouizerate, G., Durlofsky, L.J., Samier, P., 2012. New models for heater wells in subsurface simulations, with application to the in situ upgrading of oil shale. Comput. Geosci. 16 (2). https://doi.org/10.1007/s10596-011-9263-1.

Bai, F., Guo, W., Lü, X., et al., 2015. Kinetic study on the pyrolysis behavior of Huadian oil shale via non-isothermal thermogravimetric data. Fuel 146, 111–118. https://doi.org/10.1016/j.fuel.2014.12.073.

Bai, F., 2015. Theoretical and Experimental Research of Oil Shale Pyrolysis Triggered by Topochemical Heat. Jilin University.

Bai, W., Sun, Y., Guo, W., Li, Q., 2017. Pilot Test Project of Underground In-Situ Cracking of Nongan Oil Shale in Jilin Province. The 19th National Exploration Engineering Academic Exchange Conference. Urumchi, China.

Braun, R., Diaz, J., Lewis, A., 1984. Results of mathematical modeling of modified in-situ oil shale retorting. Soc. Petrol. Eng. J. 24 (1), 75–86. https://doi.org/10.2118/11000-PA.

Braun, R.L., Burnham, A.K., 1992. PMOD: a flexible model of oil and gas generation, cracking, and expulsion. Org. Geochem. 19 (1–3), 161–172. https://doi.org/10.1016/0146-6380(92)90034-U.

Burnham, A.K., 2017. Porosity and permeability of Green River oil shale and their changes during retorting. Fuel 203, 208–213. https://doi.org/10.1016/j.fuel.2017.04.119.

Burnham, A.K., McConaghy, J.R., Oct 16 - Oct 18, 2006. Comparison of the acceptability of various oil shale processes. In: 26th Oil Shale Symposium. Golden, CO, United States.

Cismondi, M., Mollerup, J., 2005. Development and application of a three-parameter RK–PR equation of state. Fluid Phase Equil. 232 (1–2), 74–89. https://doi.org/10.1016/j.fluid.2005.03.020.

Congress, 1980. An Assessment of Oil Shale Technologies. Congress, Office of Technology Assessment, United States.

Cui, G., Ren, S., Rui, Z., et al., 2018. The influence of complicated fluid-rock interactions on the geothermal exploitation in the CO_2 plume geothermal system. Appl. Energy 227, 49–63. https://doi.org/10.1016/j.apenergy.2017.10.114.

Dammer, A.R., Killen, J.C., Biglarbigi, K., et al., 2007. Secure Fuels from Domestic Resources: the Continuing Evolution of America's Oil Shale and Tar Sands Industries. Doe department of energy.

Fan, C., Zan, C., Zhang, Q., et al., 2015. Air injection for enhanced oil recovery: in situ monitoring the low-temperature oxidation of oil through thermogravimetry/differential scanning calorimetry and pressure differential scanning calorimetry. Ind. Eng. Chem. Res. 54 (26), 6634–6640. https://doi.org/10.1021/acs.iecr.5b00997.

Fan, Y., Durlofsky, L., Tchelepi, H.A., 2010. Numerical simulation of the in-situ upgrading of oil shale. SPE J. 15 (2), 368–381. https://doi.org/10.2118/118958-PA.

Fowler, T.D., Vinegar, H.J., 2009. Oil Shale ICP-Colorado Field Pilots, SPE Western Regional Meeting. Society of Petroleum Engineers. https://doi.org/10.2118/121164-MS.

Guo, H., Cheng, Q., Wang, D., et al., 2016. Analyzing the contribution of semicokes to forming self-heating in the oil-shale self-heating retorting process. Energy Fuel. 30 (7), 5355–5362. https://doi.org/10.1021/acs.energyfuels.6b00351.

Guo, W., Yang, Q., Sun, Y., et al., 2020a. Characteristics of low temperature co-current oxidizing pyrolysis of Huadian oil shale. J. Anal. Appl. Pyrol. 146, 104759. https://doi.org/10.1016/j.jaap.2019.104759.

Guo, W., Zhang, M., Sun, Y., et al., 2020b. Numerical simulation and field test of grouting in Nong'an pilot project of in-situ conversion of oil shale. J. Petrol. Sci. Eng. 184, 106477. https://doi.org/10.1016/j.petrol.2019.106477.

He, W., Sun, Y., Guo, W., et al., 2021a. Controlling the in-situ conversion process of oil shale via geochemical methods: a case study on the Fuyu oil shale, China. Fuel Process. Technol. 219, 106876. https://doi.org/10.1016/j.fuproc.2021.106876.

He, W., Sun, Y., Guo, W., et al., 2019. Organic geochemical characteristics of the upper Cretaceous Qingshankou Formation oil shales in the Fuyu oilfield, Songliao Basin, China: implications for oil-generation potential and depositional environment. Energies 12 (24), 4778. https://doi.org/10.3390/en12244778.

He, W., Sun, Y., Shan, X., 2021b. Organic matter evolution in pyrolysis experiments of oil shale under high pressure: guidance for in situ conversion of oil shale in the Songliao Basin. J. Anal. Appl. Pyrol. 155, 105091. https://doi.org/10.1016/j.jaap.2021.105091.

Kang, Z., Zhao, Y., Yang, D., 2020. Review of oil shale in-situ conversion technology. Appl. Energy 269, 115121. https://doi.org/10.1016/j.jaap.2021.105091.

Khakimova, L., Bondarenko, T., Cheremisin, A., et al., 2019. High pressure air injection kinetic model for Bazhenov Shale Formation based on a set of oxidation studies. J. Petrol. Sci. Eng. 172, 1120–1132. https://doi.org/10.1016/j.petrol.2018.09.021.

Kibodeaux, K.R., 2014. Evolution of porosity, permeability, and fluid saturations during thermal conversion of oil shale. In: SPE Annual Technical Conference and Exhibition. Society of Petroleum Engineers. https://doi.org/10.2118/170733-MS.

Langford, F., Blanc-Valleron, M.-M., 1990. Interpreting Rock-Eval pyrolysis data using graphs of pyrolizable hydrocarbons vs. total organic carbon. AAPG Bull. 74 (6), 799–804. https://doi.org/10.1306/0C9B238F-1710-11D7-8645000102C1865D.

Lee, K.J., Finsterle, S., Moridis, G.J., 2018. Analyzing the impact of reaction models on the production of hydrocarbons from thermally upgraded oil shales. J. Petrol. Sci. Eng. 168, 448–464. https://doi.org/10.1016/j.petrol.2018.05.021.

Lee, S., Speight, J.G., Loyalka, S.K., 2014. Handbook of Alternative Fuel Technologiescrc Press.

Li, H., Vink, J.C., Alpak, F.O., 2015. An efficient multiscale method for the simulation of in-situ conversion processes. SPE J. 20, 579–593. https://doi.org/10.2118/172498-PA, 03.

Li, G., Ma, Z., Zheng, J., Bao, H., et al., 2016. NMR analysis of the physical change of oil shales during in situ pyrolysis at different temperatures. Petrol. Geol. Experiment. 3, 402–406. https://doi.org/10.11781/sysydz201603402.

Liu, Z., Dong, Q., Ye, S., et al., 2009. Oil Shale of China. Petroleum Industry Press, Beijing.

Luo, Y., 2005. Chemical Bond Energy Data Sheet. Science Press, Beijing.

Ma, J., 2015. Review of permeability evolution model for fractured porous media. J. Rock Mech. Geotech. Eng. 7 (3), 351–357. https://doi.org/10.1016/j.jrmge.2014.12.003.

Meijssen, T.E., Emmen, J., Fowler, T.D., 2014. In-situ Oil Shale Development in Jordan through ICP Technology, Abu Dhabi International Petroleum Exhibition and Conference. Society of Petroleum Engineers. https://doi.org/10.2118/172135-MS.

Ojha, S.P., Misra, S., Tinni, A., et al., 2017. Relative permeability estimates for Wolfcamp and Eagle Ford shale samples from oil, gas and condensate windows using adsorption-desorption measurements. Fuel 208, 52–64. https://doi.org/10.1016/j.fuel.2017.07.003.

Pei, S., Wang, Y., Zhang, L., et al., 2018. An innovative nitrogen injection assisted in-situ conversion process for oil shale recovery: mechanism and reservoir simulation study. J. Petrol. Sci. Eng. 171, 507–515. https://doi.org/10.1016/j.petrol.2018.07.071.

Peng, S., Guo, H., Zhou, J., et al., 2013. Study on the influencing factors of oil shale retorting with low-temperature oxygen-containing carrier gas. Contemp. Chem. Ind. 42 (7), 885–888.

Sang, Q., Zhang, S., Li, Y., et al., 2018. Determination of organic and inorganic hydrocarbon saturations and effective porosities in shale using vacuum-imbibition method. Int. J. Coal Geol. 200, 123–134. https://doi.org/10.1016/j.coal.2018.10.010.

Skinner, H., Pilcher, G., 1963. Bond-energy term values in hydrocarbons and related compounds. Q. Rev. Chem. Soc. 17 (3), 264–288.

Sun, Y., Bai, F., Lü, X., et al., 2015a. Kinetic study of Huadian oil shale combustion using a multi-stage parallel reaction model. Energy 82, 705–713. https://doi.org/10.1016/j.energy.2015.01.080.

Sun, Y., Bai, F., Lü, X., et al., 2015b. A novel energy-efficient pyrolysis process: self-pyrolysis of oil shale triggered by topochemical heat in a horizontal fixed bed. Sci. Rep. 5 (1), 1–8. https://doi.org/10.1038/srep08290.

Sun, Y., Guo, W., Deng, S., 2021. The status and development trend of in-situ conversion and drilling exploitation technology for oil shale. Drilling Eng. 48 (1), 57–67. https://doi.org/10.12143/j.ztgc.2021.01.008.

Tong, J., Han, X., Wang, S., et al., 2011. Evaluation of structural characteristics of Huadian oil shale kerogen using direct techniques (solid-state 13C NMR, XPS, FT-IR, and XRD). Energy Fuel. 25 (9), 4006–4013. https://doi.org/10.1021/ef200738p.

Wang, D., Ren, Y., Wang, M., et al., 2018. Study on the mechanism of oil-shale aerobic retorting process. Contemp. Chem. Ind. 47 (2), 247–251. https://doi.org/10.13840/j.cnki.cn21-1457/tq.2018.02.008.

Wang, G., Yang, D., Kang, Z., et al., 2018a. Anisotropy in thermal recovery of oil shale—Part 1: thermal conductivity, wave velocity and crack propagation. Energies 11 (1), 77. https://doi.org/10.3390/en11010077.

Wang, G., Yang, D., Zhao, Y., et al., 2019. Experimental investigation on anisotropic permeability and its relationship with anisotropic thermal cracking of oil shale under high temperature and triaxial stress. Appl. Therm. Eng. 146, 718–725. https://doi.org/10.1016/j.applthermaleng.2018.10.005.

Wang, Y., Ren, S., Zhang, L., et al., 2018b. Numerical study of air assisted cyclic steam stimulation process for heavy oil reservoirs: recovery performance and energy efficiency analysis. Fuel 211, 471–483. https://doi.org/10.1016/j.fuel.2017.09.079.

Wang, Y., Wang, Y., Meng, X., et al., 2013. Enlightenment of American's oil shale in-situ retorting technology. Oil Dril. Prod. Technol. 35 (6), 55–59.

Yuan, C., Varfolomeev, M.A., Emelianov, D.A., et al., 2018. Oxidation behavior of light crude oil and its SARA fractions characterized by TG and DSC techniques: differences and connections. Energy Fuel. 32 (1), 801–808. https://doi.org/10.1021/acs.energyfuels.7b02377.

Zheng, H., Shi, W., Ding, D., et al., 2017. Numerical simulation of in situ combustion of oil shale. Geofluids 2017 (3028974), 1–9. https://doi.org/10.1155/2017/3028974.

Zhu, C., Sheng, J.J., Ettehadtavakkol, A., et al., 2019. Numerical and experimental study of enhanced shale-oil recovery by CO2 miscible displacement with NMR. Energy Fuel. 34 (2), 1524–1536. https://doi.org/10.1021/acs.energyfuels.9b03613.

Zou, C., Qiu, Z., 2021. Preface: new advances in unconventional petroleum sedimentology in China. Acta Sedimentol. Sin. 39 (1), 38–46. https://doi.org/10.14027/j.issn.1000-0550.2021.001.